Mechanisms of ventricular rate adaptation as a predictor of arrhythmic risk

Esther Pueyo,[1,2,3] Zoltán Husti,[4] Tibor Hornyik,[4,5] István Baczkó,[4] Pablo Laguna,[2,3] András Varró,[4,5] and Blanca Rodríguez[1]

[1]*Oxford University Computing Laboratory, University of Oxford, Oxford, United Kingdom;* [2]*Instituto de Investigación en Ingeniería de Aragón, Universidad de Zaragoza, Zaragoza, Spain;* [3]*Centro de Investigación Biomédica En Red de Bioingeniería, Biomateriales y Nanomedicina, Zaragoza, Spain;* and [4]*Department of Pharmacology and Pharmacotherapy, University of Szeged,* and [5]*Research Unit for Cardiovascular Pharmacology, Hungarian Academy of Sciences, Szeged, Hungary*

Pueyo E, Husti Z, Hornyik T, Baczkó I, Laguna P, Varró A, Rodríguez B. Mechanisms of ventricular rate adaptation as a predictor of arrhythmic risk. *Am J Physiol Heart Circ Physiol* 298: H1577–H1587, 2010. First published March 5, 2010; doi:10.1152/ajpheart.00936.2009.—Protracted QT interval (QTI) adaptation to abrupt heart rate (HR) changes has been identified as a clinical arrhythmic risk marker. This study investigates the ionic mechanisms of QTI rate adaptation and its relationship to arrhythmic risk. Computer simulations and experimental recordings in human and canine ventricular tissue were used to investigate the ionic basis of QTI and action potential duration (APD) to abrupt changes in HR with a protocol commonly used in clinical studies. The time for 90% QTI adaptation is 3.5 min in simulations, in agreement with experimental and clinical data in humans. APD adaptation follows similar dynamics, being faster in midmyocardial cells (2.5 min) than in endocardial and epicardial cells (3.5 min). Both QTI and APD adapt in two phases following an abrupt HR change: a fast initial phase with time constant < 30 s, mainly related to L-type calcium and slow-delayed rectifier potassium current, and a second slow phase of >2 min driven by intracellular sodium concentration ($[Na^+]_i$) dynamics. Alterations in $[Na^+]_i$ dynamics due to Na^+/K^+ pump current inhibition result in protracted rate adaptation and are associated with increased proarrhythmic risk, as indicated by action potential triangulation and faster L-type calcium current recovery from inactivation, leading to the formation of early afterdepolarizations. In conclusion, this study suggests that protracted QTI adaptation could be an indicator of altered $[Na^+]_i$ dynamics following Na^+/K^+ pump inhibition as it occurs in patients with ischemia or heart failure. An increased risk of cardiac arrhythmias in patients with protracted rate adaptation may be due to an increased risk of early afterdepolarization formation.

action potentials; ventricles; ion channels; arrhythmia; computers

CLINICAL, EXPERIMENTAL, AND theoretical studies have shown that an abrupt change in heart rate (HR) results in the progressive adaptation of the QT interval (QTI) in the ECG because of short-term cardiac memory effects (2, 3, 22, 29, 35, 36). Patients exhibiting protracted QTI HR adaptation dynamics have been identified as at increased risk of experiencing cardiac arrhythmias and sudden cardiac death (22, 35). Furthermore, clinical data also suggest that the extent of amiodarone-induced acceleration of QTI HR adaptation could be used as a therapeutic marker of drug efficacy (37). However, despite strong evidence suggesting an important role of short-term cardiac memory in arrhythmogenesis, the underlying mechanisms are still controversial.

The present study investigates the ionic basis of QTI rate adaptation in human ventricular tissue and its link to proarrhythmic mechanisms. Computer simulations and experiments were conducted to identify the specific mechanisms of ionic transport that determine QTI rate adaptation and how alterations in those mechanisms might result in arrhythmic events. Key simulation predictions were evaluated using experimental and clinical data from the literature and a limited set of experiments in humans performed in this study. Ionic mechanisms underlying HR adaptation were further investigated using simulations and experiments in both humans and dogs because of their similar repolarization mechanisms and the greater availability of canine tissue compared with that of humans (41).

MATERIALS AND METHODS

Computer Modeling and Simulation

Human (38) and canine (10) ventricular cell models were used to investigate short-term memory mechanisms. Computer simulations of electrical propagation and pseudo-ECG (pECG) (21) were conducted using a transmural one-dimensional fiber model, consisting of 100 cells [30% endocardial (Endo), 30% midmyocardial (Mid), and 40% epicardial (Epi) cells (12, 38)]. A 1-ms square stimulus pulse of 1.5 times diastolic threshold was applied to the endocardium. Integration was performed using the forward Euler method with a 0.02-ms time step and 0.015-cm space step. pECG peaks and boundaries were identified using an automatic wavelet transform-based delineation system (33). pECG QTI was measured as the time interval between the QRS complex onset and the T-wave end.

Characterization of Ventricular HR Adaptation Dynamics

The rate adaptation of QTI and action potential (AP) duration (APD) at 90% repolarization was evaluated (18, 29): pacing at a cycle length (CL) of 1,000 ms was applied until steady state, followed by a CL of 600 ms for 10 min and back to a CL of 1,000 ms for an additional 10 min. Fast and slow phases in QTI and APD rate adaptation were identified, and time constants (τ) of their dynamics were obtained by fitting to: $f(t) = a + be^{-(t-c)/\tau}$.

Time constants τ_{fast} and τ_{slow}, characterizing each of the two adaptation phases, were obtained, both after the CL increase and decrease. In cases where the fast phase consisted of only two data points, then $f(t) = be^{-t/\tau}$ was used to derive τ_{fast}.

QTI or APD adaptation is defined as protracted when the associated time constant τ_{slow} is abnormally long (see RESULTS for a detailed description), which is related to irregularities in APD adaptation dynamics and the generation of afterdepolarizations.

Evaluation of Proarrhythmic Risk in Simulation

To investigate the ionic mechanisms of rate adaptation and its relationship to risk, adaptation dynamics and arrhythmic risk markers

Address for reprint requests and other correspondence: E. Pueyo, Oxford Univ. Computing Lab., Wolfson Bldg., Parks Rd., Oxford OX1 3QD, UK (e-mail: epueyo@unizar.es).

were quantified for control and also following ± 15 and $\pm 30\%$ changes in specific model parameters. The arrhythmic risk markers (30) considered were 1) AP triangulation, quantified as $\delta = \text{APD}/\text{APD}_{50}$, where APD_{50} denotes APD at 50% repolarization, considered to be an indicator of an early afterdepolarization (EAD) occurrence (34); 2) APD restitution (APDR) curve slope at a diastolic interval of 60 ms (26), determined using both S1-S2 and dynamic protocols (38), $S_{\text{S1-S2}}$ and S_{dyn}, respectively; and 3) calcium current reactivation, as the product ρ of the inactivation gates [f, f_2, and f_{cass} (38)] of the L-type calcium current (I_{CaL}) computed at 90% repolarization for steady state at a CL of 1,000 ms (42).

Experimental Methods

Experiments were performed to validate key simulation results, when specific data were not available in the literature. Experiments were conducted in human ventricular tissue when available ($n = 2$ tissue samples); otherwise, right ventricle papillary muscles isolated from adult mongrel dogs hearts ($n = 21$) were used (8–20 kg, either sex) (40). All animal experiments were conducted in compliance with the *Guide for the Care and Use of Laboratory Animals* (NIH Publication No. 85-23, Revised 1996), and the protocol was approved by the Ethical Committee for the Protection of Animals in Research of the University of Szeged, Hungary (I-74-125-2007) and by the Department of Animal Health and Food Control of the Ministry of Agriculture and Rural Development (XIII/01031/000/2008). Regarding human experiments, undiseased human hearts that were technically not usable for transplantation (based on logistical and not on patient-related reasons) were obtained from general organ donors. Before cardiac explantation, organ donor patients did not receive medication except dobutamine, furosemide, and plasma expanders. The investigations conform with the principles outlined in the *Declaration of Helsinki* of the World Medical Association. The experimental procedures and protocols were approved by the Ethical Review Board of the Medical Center of the University of Szeged, Hungary (No. 51-57/1997 OEJ). Human right ventricular papillary muscle preparations were dissected from donor hearts stored in cardioplegic solution at 4°C for 3 to 4 h before placing them into oxygenated modified Locke's solution containing (in mM) 120 NaCl, 4 KCl, 1.0 CaCl₂, 1 MgCl₂, 22 NaHCO₃, and 11 glucose. The pH of this solution was set to 7.4 ± 0.05 when saturated with the mixture of 95% O_2 and 5% CO_2 at 37°C.

Transmembrane APs were recorded using the conventional microelectrode technique as described previously (40). APD HR adaptation was evaluated using the same protocol as in the simulations, both in control (in humans and dogs) and in the presence of the following drug concentrations (in dogs): 0.2 and 0.6 µM strophanthin G ($n = 5$ and 7), 1 and 3 µM nisoldipine ($n = 1$), 30 µM BaCl₂ ($n = 2$), 0.25 µM HMR-1556 ($n = 3$), and 0.1 µM dofetilide ($n = 3$). Strophanthin G and BaCl₂ were dissolved in distilled water to give stock solution concentrations of 1 and 50 mM, respectively. Nisoldipine was dissolved in 100% ethanol stock solution (1 mM). HMR-1556 was dissolved in DMSO stock solution (1 mM).

RESULTS

Ventricular Rate Adaptation

QTI adaptation. Figure 1*A* illustrates QTI adaptation kinetics in humans from simulations (*left*) and clinical data (29) (*right*). Figure 1*B* shows simulated pECG for the first beat following HR acceleration (*left*) and deceleration (*right*) and when the new steady state is reached. QTI adaptation after a
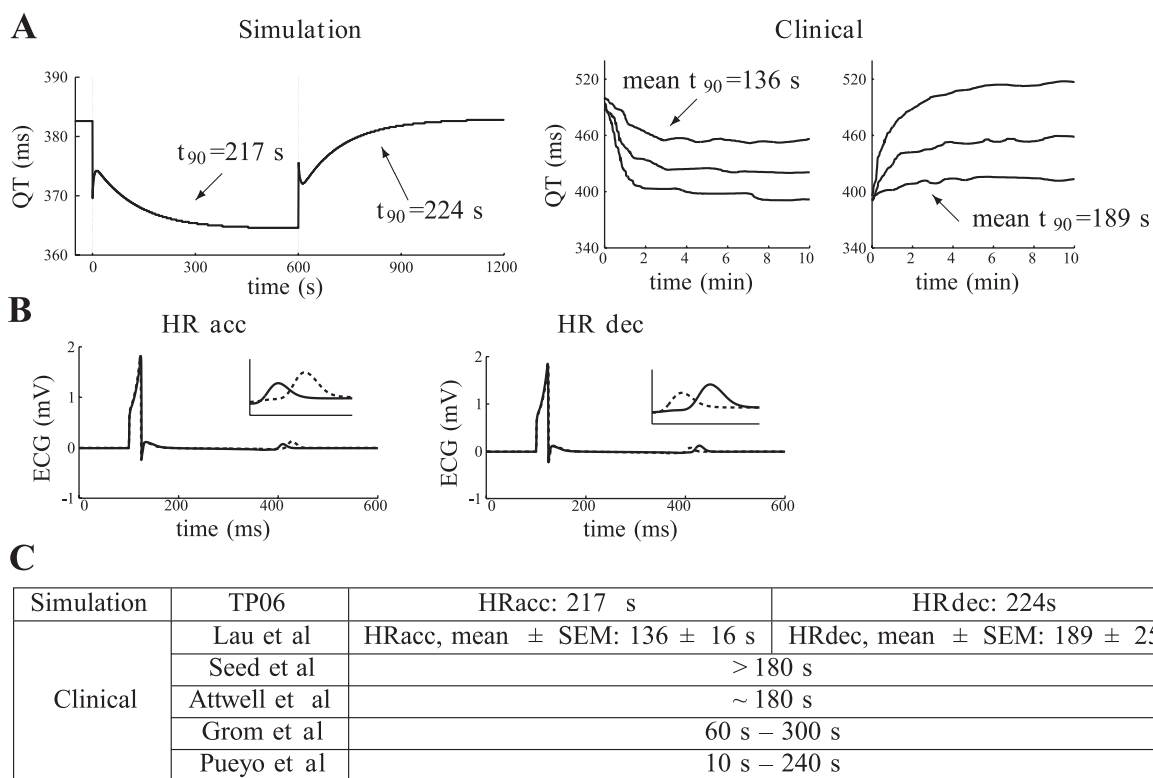

A　Simulation　　　　　　　　Clinical

B　HR acc　　　　HR dec

C

Simulation	TP06	HRacc: 217 s	HRdec: 224s
Clinical	Lau et al	HRacc, mean ± SEM: 136 ± 16 s	HRdec, mean ± SEM: 189 ± 25 s
	Seed et al	> 180 s	
	Attwell et al	~ 180 s	
	Grom et al	60 s – 300 s	
	Pueyo et al	10 s – 240 s	

Fig. 1. *A*, *left*: simulated QT interval (QTI) adaptation in human pseudo-ECG for cycle length (CL) of 1,000 to 600 to 1,000 ms. *A*, *right*: QTI adaptation in human ECG recordings for 50 or 110 beats/min in increments or decrements of 20, 40, and 60 beats/min (modified and redrawn from original graphs from Ref. 29). Time required for 90% QTI rate adaptation (t_{90}) is presented. *B*: simulated pseudo-ECGs corresponding to first (dotted line) and last (solid line) beats after CL decrease (*left*) and CL increase (*right*). *C*: t_{90} values for simulated pseudo-ECGs and clinical human ECGs. HR, heart rate; Acc, acceleration; Dec, deceleration; TP06, human ventricular cell model developed by ten Tusscher and Panfilov (38) in 2006.

step CL decrease/increase begins with a fast QTI shortening/lengthening during the initial beats after the HR change ($\tau_{fast} = 17/34$ s), followed by a second slow accommodation ($\tau_{slow} = 122/122$ s). In the simulations, the time (t_{90}) required for QTI to complete 90% of its adaptation in humans is 217/224 s following HR acceleration/deceleration. As shown in Fig. 1*C*, simulation values for t_{90} are within the wide range reported clinically.

A sensitivity analysis was performed to assess the dependence of QTI rate adaptation dynamics on CL change magni-

tude (m_{CL}) and on the initial CL (i_{CL}). Values for m_{CL} considered were 200, 400, and 600 ms, and values for i_{CL} were 1,000 and 1,400 ms. No statistically significant differences (analysis of variance, $P > 0.05$) in t_{90} are observed when varying m_{CL} or i_{CL}.

APD adaptation. Figure 2, *A* and *B*, illustrates APD HR adaptation in simulated Endo (*top*), Mid (*middle*), and Epi (*bottom*) human ventricular cells. Figure 2*A* shows the time course of APD adaptation, and Fig. 2*B* illustrates the AP corresponding to the first beat and the new steady state follow-

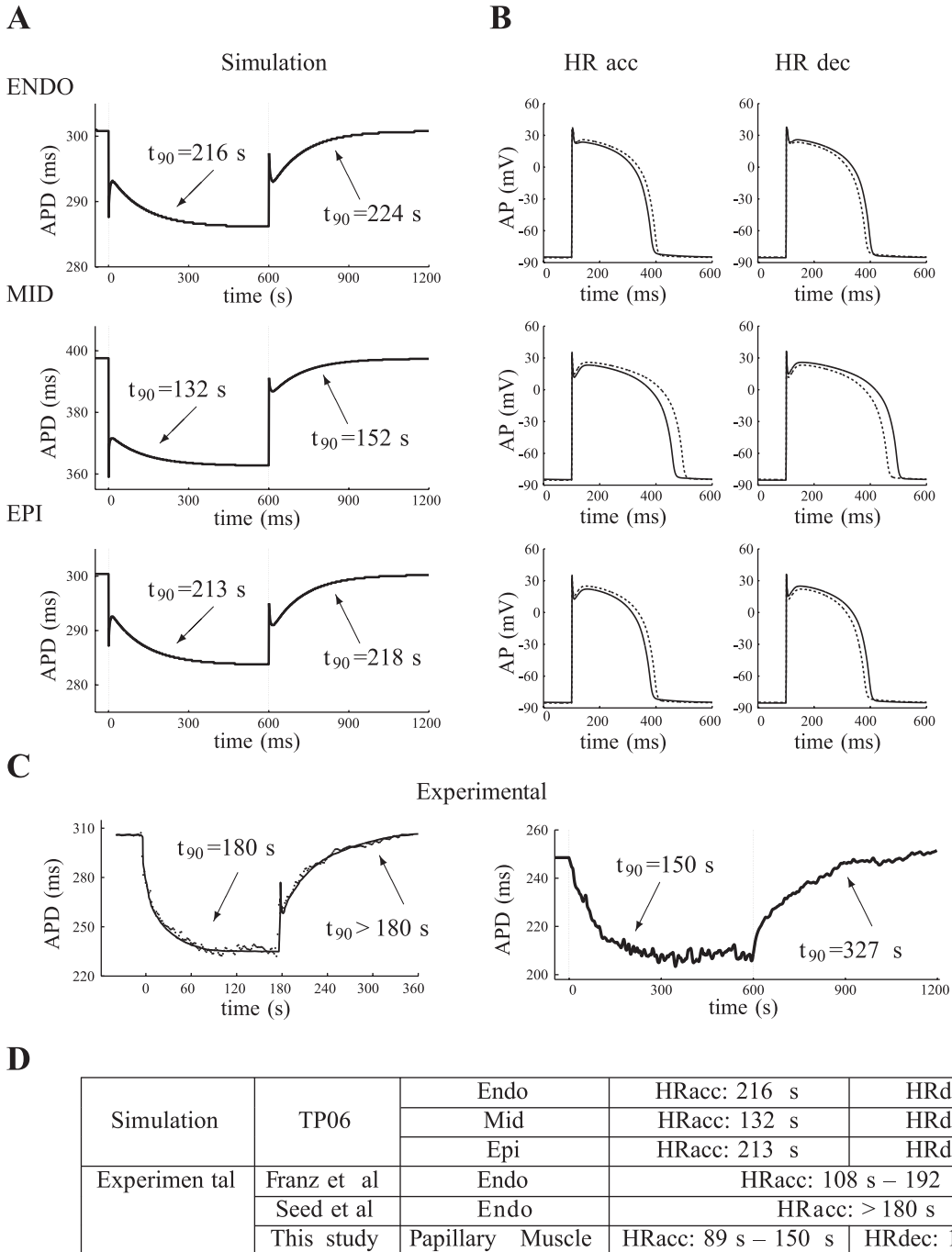| Simulation	TP06	Endo	HRacc: 216 s	HRdec: 224 s
		Mid	HRacc: 132 s	HRdec: 152 s
		Epi	HRacc: 213 s	HRdec: 218 s
Experimental	Franz et al	Endo	HRacc: 108 s – 192 s	
	Seed et al	Endo	HRacc: > 180 s	
	This study	Papillary Muscle	HRacc: 89 s – 150 s	HRdec: 159 s – 327 s

Fig. 2. *A*: simulated action potential (AP) duration (APD) adaptation in humans for CL of 1,000 to 600 to 1,000 ms for endocardial (Endo; *top*), midmyocardial (Mid; *middle*), and epicardial (Epi; *bottom*) cardiomyocytes. *B*: simulated APs corresponding to first (dotted line) and last (solid line) beats after CL decrease (*left*) and CL increase (*right*) for human Endo (*top*), Mid (*middle*), and Epi (*bottom*) cardiomyocytes. *C*: experimental APD adaptation in humans for CL of 750–410 ms (*left*, modified and redrawn from original graphs from Ref. 18) and for CL of 1,000–600 ms (*right*, this study). *D*: t_{90} values for simulated and experimental human APs.

ing HR acceleration (*left*) and deceleration (*right*) for the three cell types. Figure 2*C* presents experimental APD adaptation measured in human ventricular endocardium (18), as well as in human papillary muscle, measured in this study.

It is clear that APD HR adaptation dynamics are similar in human simulations and experiments (18) and comparable with QTI HR adaptation dynamics (shown in Fig. 1), consisting of a fast and slow phase (τ_{fast} = 13/26 s after CL decrease/increase for Endo, 6/14 s for Mid, and 13/26 s for Epi cells; and τ_{slow} = 126/122 s after CL decrease/increase for Endo, 128/122 s for Mid, and 126/123 s for Epi cells). This suggests that QTI HR adaptation is a manifestation of cellular APD HR adaptation. As shown in Fig. 2*D*, simulation values for t_{90} are within the range observed experimentally. Furthermore, simulations with both the human and the dog models yield similar rate adaptation dynamics, although slightly slower in dog (t_{90} = 282/311 s in canine and t_{90} = 213/218 s in human Epi cells for HR acceleration/deceleration, respectively). Analogous to the results reported for QTI in this study, no statistically significant differences in t_{90} for APD adaptation are found when varying m_{CL} or i_{CL}.

Ionic Mechanisms of APD Rate Adaptation

Figures 3 and 4 illustrate the ionic mechanisms of APD HR adaptation in humans. Each panel in Fig. 3 represents the change in peak value of each ionic current [slow delayed rectifier potassium current (I_{Ks}), I_{CaL}, transient outward potassium current (I_{to}), rapid delayed rectifier potassium current (I_{Kr}), inward rectifier potassium current (I_{K1}), fast sodium current (I_{Na}), Na^+/Ca^{2+} exchanger current (I_{NaCa}), and Na^+/K^+ pump current (I_{NaK})] or intracellular sodium and calcium ion concentration ([Na^+]$_i$ and [Ca^{2+}]$_i$), as a function of APD for the beats following HR acceleration (analogous results were obtained for HR deceleration; graphics not shown). The numbers shown in each graph indicate the number of beats following the CL change. Bar graphs in Fig. 4 show the percentage of total change in peak values of each ionic current or intracellular ion concentration that occurred during the fast (*top*) and slow (*bottom*) phase of HR adaptation. The ionic mechanisms involved in each of the adaptation phases, fast and slow, are further described in the following.

Initial fast phase of adaptation. Figures 3 and 4 show that I_{CaL} and I_{Ks} experience the greatest percentage of total change during the initial phase of rate adaptation and are key mechanisms driving that phase. Other ionic currents, such as I_{to}, present a percentage of change similar to I_{Ks}, but these changes are a consequence (and not a cause) of APD adaptation, since variations in conductance and/or kinetics do not affect τ_{fast}.

Figure 5*A* further illustrates the role that the dynamics of the I_{CaL} slow voltage-dependent inactivation gate (*f*) and the I_{Ks}
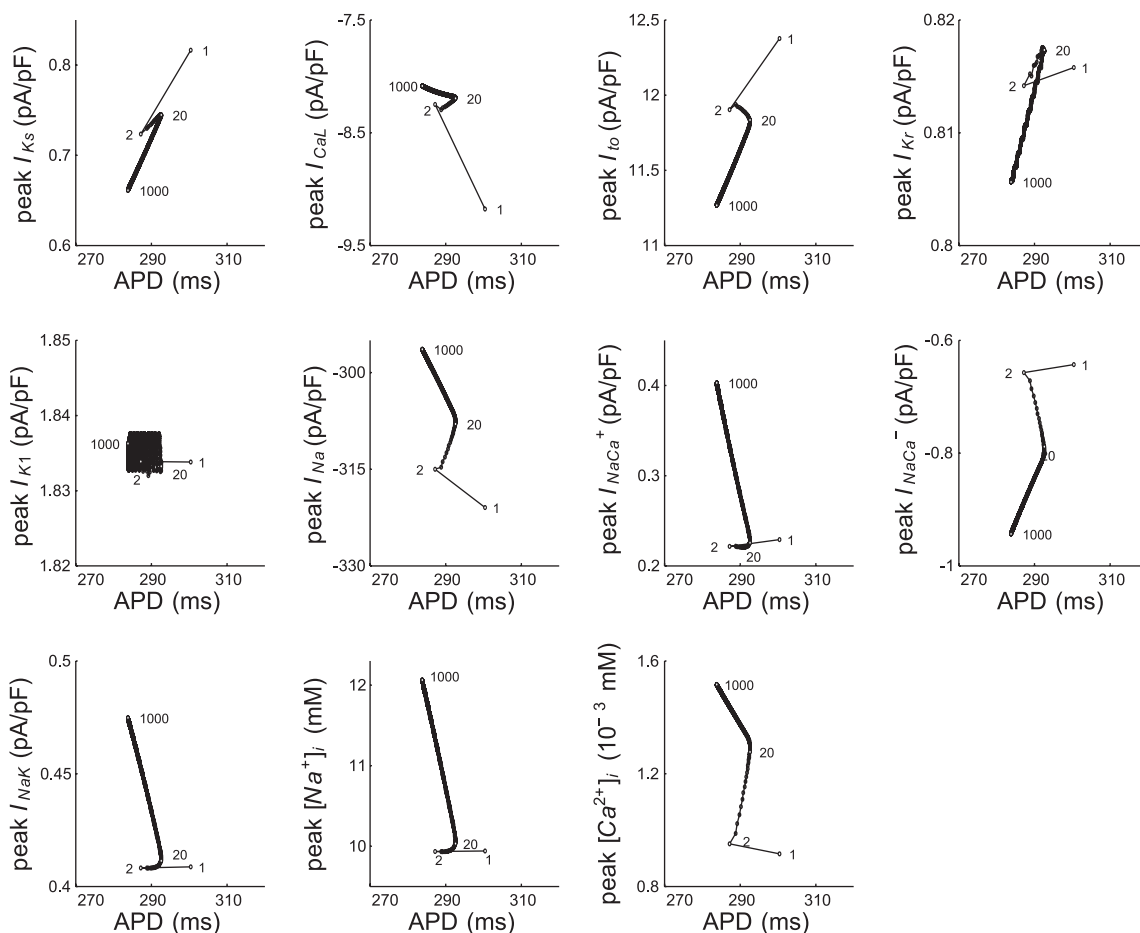

Fig. 3. Peak values for I_{Ks}, I_{CaL}, I_{to}, I_{Kr}, I_{K1}, I_{Na}, I_{NaCa}, I_{NaK}, [Na^+]$_i$, and [Ca^{2+}]$_i$ (see main text for definitions of abbreviations) as a function of APD during adaptation for CL varying from 1,000 to 600 ms in humans. Beat number after step CL change is shown.
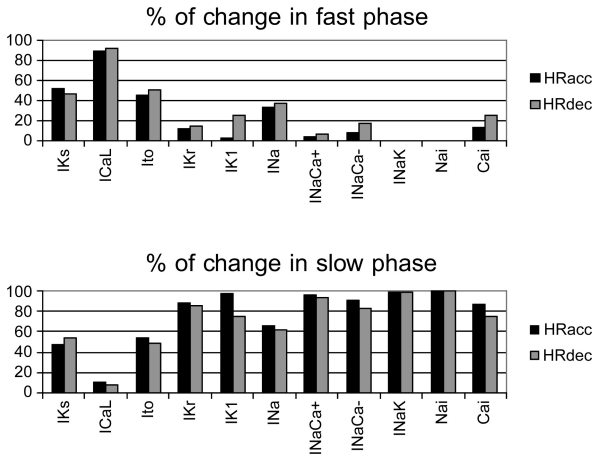
Fig. 4. Percentage of total change in peak value for each ionic current and concentration during fast (*top*) and slow (*bottom*) phases of APD adaptation for CL varying from 1,000 to 600 ms (HRacc) and from 600 to 1,000 ms (HRdec). Nai, $[Na^+]_i$; Cai, $[Ca^{2+}]_i$.

activation gate (*xs*) play in the fast phase of human APD adaptation. Indeed, a sudden decrease in CL results in an insufficient time for *f* to fully recover ($f < 1$) (Fig. 5A, *top*), whereas I_{Ks} is unable to completely deactivate ($xs > 0$) at the end of each beat. The resulting decrease in inward and increase in outward currents contribute to APD shortening following HR acceleration. To further illustrate the importance of *f* and *xs* in the initial adaptation phase, Fig. 5A, *right*, shows APD adaptation dynamics for control and for a simulation where beat-to-beat differences in *f* and *xs* are eliminated by fixing them to their steady-state values for a CL of 1,000 ms ($f = 0.9774$ and $xs = 0.003225$, respectively). Results show that eliminating beat-to-beat differences in *f* and *xs* leads to the abolishment of the fast phase of APD adaptation. Similar mechanisms are observed using the canine ventricular model (not shown).

Simulations were performed to evaluate the effect of moderate changes (± 15–30%) in values of key parameters defining gate kinetics and conductances of all ionic currents in the human ventricular model. The effect of those changes on time constants for the fast and slow adaptation phases (τ_{fast} and τ_{slow}), as well as the arrhythmic risk indicators ρ, δ, S_{S1-S2}, and S_{dyn}, were quantified. Simulation results are shown in Fig. 6 for the parameters with greatest influence on human APD HR adaptation. As previously discussed and illustrated in Figs. 3–5, Fig. 6 (*first row*) also shows that τ_{fast} is greatly sensitive to I_{CaL} inactivation and I_{Ks} activation kinetics and thus moderate changes of up to 30% in τ_f and τ_{xs} significantly alter τ_{fast}. Changes of up to 30% in ionic current conductances have only a negligible effect on τ_{fast} (Fig. 6, *first row*). Additional simulations and experiments were conducted to evaluate whether large degrees (>70%) of ion channel block could affect τ_{fast}. Results for human ventricular myocyte simulations and canine experiments are shown in Fig. 7, *left* and *right*, respectively, for I_{CaL} (*A*), I_{Ks} (*B*), I_{K1} (*C*), and I_{Kr} (*D*). Results show that I_{CaL} block by 70–90% significantly increases τ_{fast} by 54–249/107–223% following HR acceleration/deceleration using the human model (Fig. 7A, *left*). Qualitatively similar results are obtained using the canine model (not shown), although the effects are more pronounced in dogs, reaching >500% change in τ_{fast} for full I_{CaL} block. In the experiments, I_{CaL} block using 1 or 3 µM nisoldipine also results in increased τ_{fast} in canine papillary muscle (Fig. 7A, *right*), although to a lower extent than in the simulations, i.e., by 33/72% and 54/94% following HR acceleration/deceleration, respectively.

Furthermore, simulated 90–100% I_{Ks} inhibition results in a significant decrease in τ_{fast} by 71–82/63–76% following HR acceleration/deceleration in humans (Fig. 7B, *left*), whereas in dogs, the simulated effect is <10%. In the canine experiments, I_{Ks} block by 0.25 µM HMR-1556 (~full block) led to 16/20% decrease in τ_{fast} following HR acceleration/deceleration (Fig. 7B, *right*). The effect of I_{K1} and I_{Kr} block on τ_{fast} was also explored. The results in Fig. 7C, *left*, show that simulated I_{K1} block by 80–90% results in a 6–40/3–22% increase in τ_{fast} following HR acceleration/deceleration in humans, whereas in dogs it results in a 39–67/41–67% decrease in τ_{fast}. In the experiments, 30 µM $BaCl_2$ (estimated 80% block) results in a 28/11% decrease in τ_{fast} (Fig. 7C, *right*). Full I_{Kr} block results in a 7/9% increase in τ_{fast} with the human model (Fig. 7D, *left*), but in the canine model this leads to EADs, making the τ_{fast} measurement impossible. In the canine experiments with 0.1 µM dofetilide, there is a 10/10% decrease in τ_{fast} following HR acceleration/deceleration (Fig. 7D, *right*). Overall, the simulations and experiments show a good qualitative agreement in the
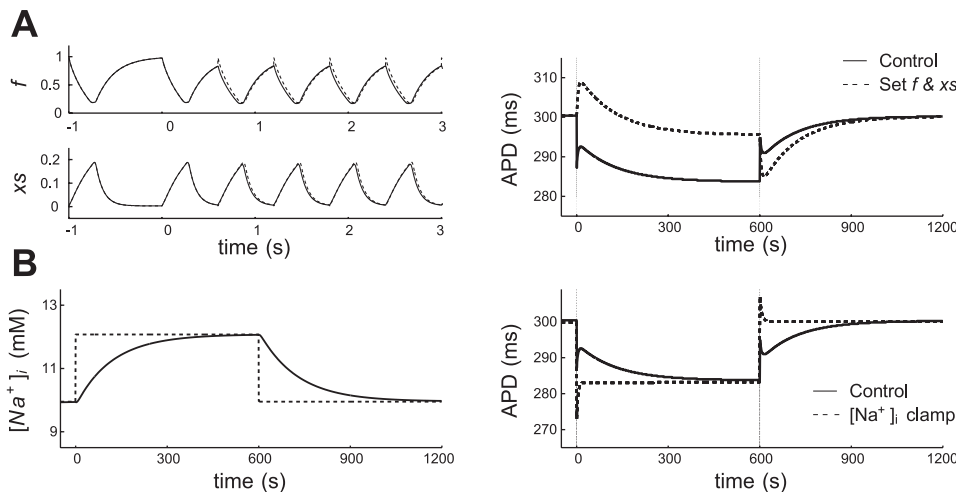

Fig. 5. Mechanisms of the fast and slow phases of APD adaptation after abrupt sustained CL changes (1,000 to 600 to 1,000 ms) in humans. *A*, *left*: time course of the I_{CaL} slow voltage-dependent inactivation gate *f* and the I_{Ks} activation gate *xs* for the first 5 beats after CL decrease for control (solid line) and when gate variables are preset to the steady-state value for CL of 1,000 ms at the beginning of each beat (dotted line). *A*, *right*: corresponding APD time courses. *B*, *left*: time course of $[Na^+]_i$ for control (solid line) and when clamped to its steady-state value for each CL (dotted line). *B*, *right*: corresponding APD time courses.
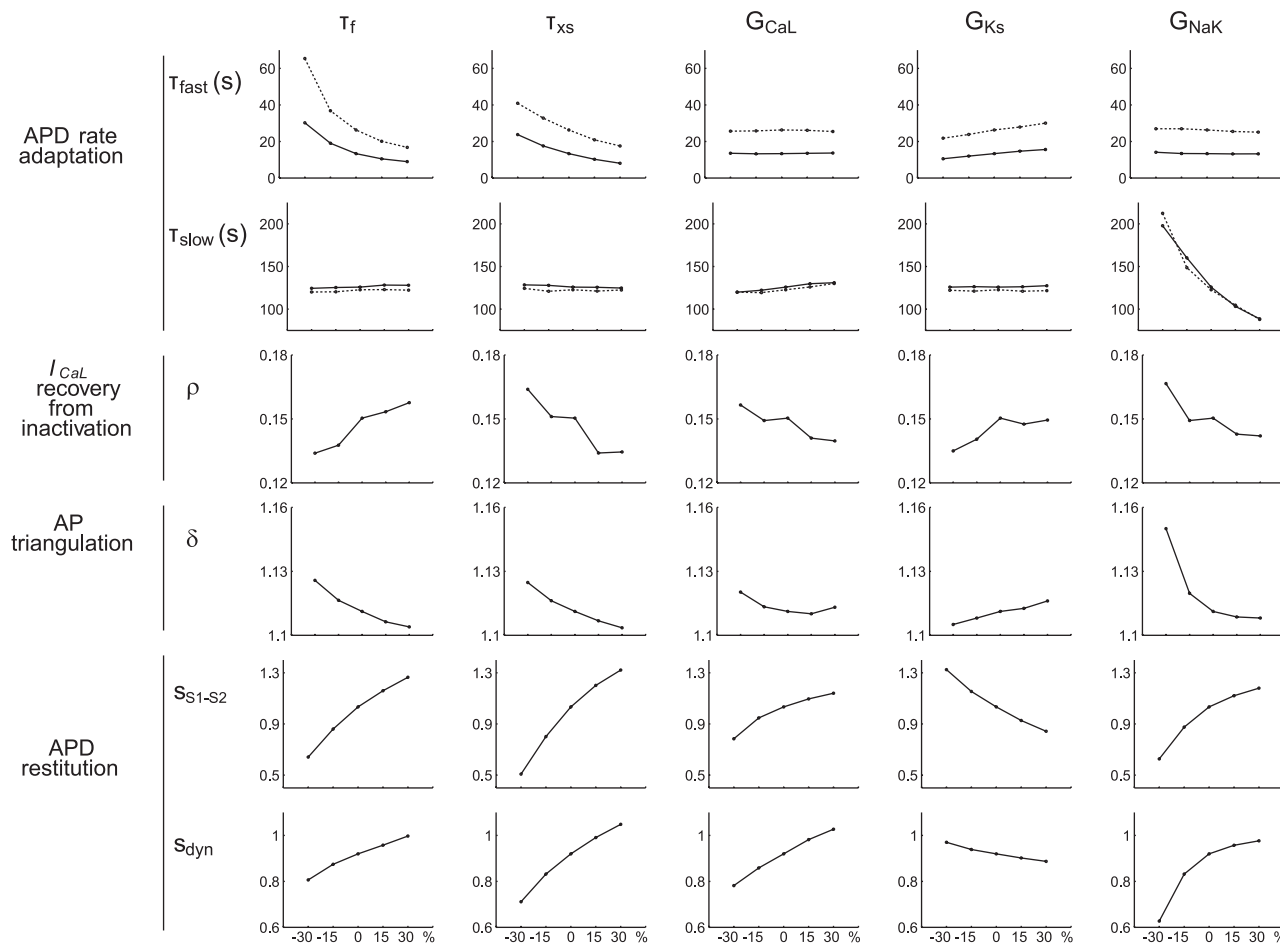
Fig. 6. Changes in time constants for fast (τ_{fast}, *first row*) and slow (τ_{slow}, *second row*) phases of APD adaptation (solid line for HR acceleration for CL of 1,000 to 600 ms, and dotted line for HR deceleration for CL of 600 to 1000 ms), degree of I_{CaL} recovery from inactivation at 90% repolarization (ρ, *third row*), AP triangulation (δ, *fourth row*), S1-S2 restitution slope ($S_{S1\text{-}S2}$, *fifth row*), and dynamic restitution slope (S_{dyn}, *sixth row*) induced by $\pm$ 15–30% variations in time constant of slow voltage-dependent I_{CaL} inactivation gate f (τ_f, *first column*), time constant of I_{Ks} activation gate xs (τ_{xs}, *second column*), I_{CaL} maximal conductance (G_{CaL}, *third column*), I_{Ks} maximal conductance (G_{Ks}, *fourth column*), and maximal I_{NaK} (G_{NaK}, *fifth column*).

effect of specific ionic current block on τ_{fast}, although specific quantitative differences are found, which are further analyzed in DISCUSSION.

Slow phase of adaptation. APD adaptation finishes with a slow phase, during which $[Na^+]_i$ and $[Ca^{2+}]_i$, as well as I_{NaK}, I_{NaCa}, and several potassium currents, experience important changes (Figs. 3 and 4). As shown in Fig. 5B, *left*, following HR acceleration, $[Na^+]_i$ slowly accumulates (control trace), which causes an increase in repolarization current via enhanced activity of I_{NaK} and I_{NaCa} (operating in reverse mode), resulting in a progressive APD shortening. With the use of both human and canine ventricular models, clamping $[Na^+]_i$ to its steady-state value eliminates the slow APD adaptation phase (Fig. 5B, $[Na^+]_i$ clamp in humans). This suggests that $[Na^+]_i$ dynamics determine the slow phase of adaptation and that changes in potassium currents depicted in Figs. 3 and 4 are secondary to APD alterations caused by sodium regulation.

The results in Fig. 6 confirm the importance of I_{NaK} in the slow phase of APD adaptation: I_{NaK} maximal conductance is the only model parameter that when altered moderately (up to 30%) exerts a significant influence in τ_{slow} in both humans and dogs. Figure 8A shows that I_{NaK} inhibition by 30% results in an increase in τ_{slow} by ~60% in virtual humans (Fig. 8A, *left*) and

by ~150% in virtual canine Epi myocytes, whereas 0.6 μM strophanthin G results in an ~100% increase in τ_{slow} in canine experiments (Fig. 8A, *right*). I_{K1} and I_{Kr} block are also found to have an impact on the slow APD adaptation, although only in dogs, not in humans, and only for almost complete block. Specifically, 90% I_{K1} block leads to a >30% decrease in τ_{slow} in both simulations and experiments in dogs but only to a ~10% decrease in human simulations. Full I_{Kr} block is associated with >25% increase in τ_{slow} in experiments in dogs but results in <10% change in τ_{slow} in humans. The effects of I_{CaL} or I_{Ks} block on τ_{slow} are negligible.

APD HR Adaptation and Arrhythmic Risk

In this section, the link between protracted QTI and APD HR adaptation dynamics and arrhythmic risk suggested by clinical studies (19, 35) is investigated. As shown in Fig. 6, fast I_{CaL} inactivation and I_{Ks} activation (i.e., decrease in τ_f or τ_{xs}, respectively) lead to large τ_{fast} values and to a simultaneously flattening of restitution curves, an enhanced AP triangulation (associated with increased risk of EAD development), and a decrease and an increase in ρ, respectively (protection against and increased likelihood of I_{CaL} reactivation during AP repo-
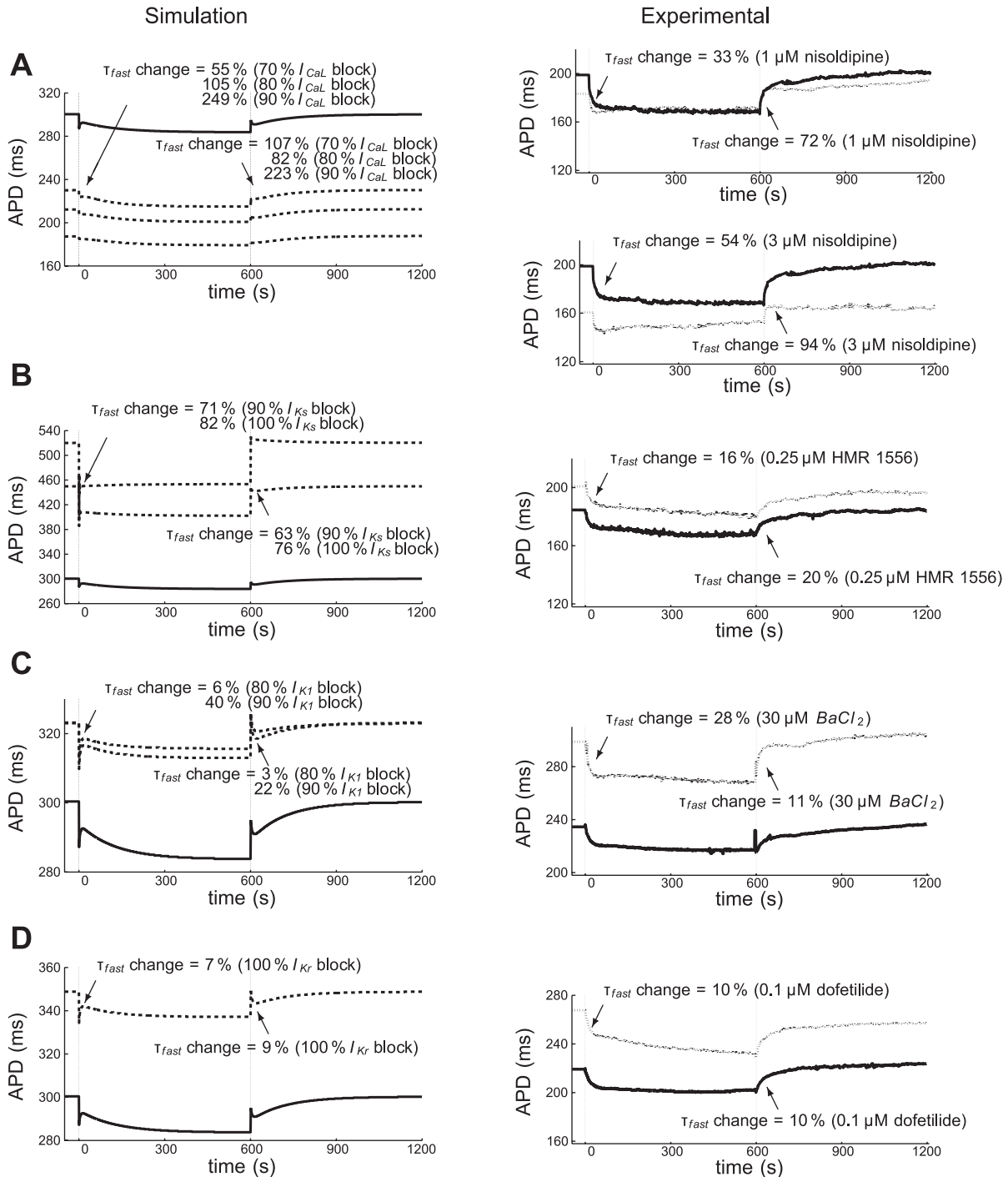
Fig. 7. Effect of ion channel block on APD rate adaptation dynamics. *Left*: simulation results in human ventricular cardiomyocyte. *Right*: experimental recordings in canine papillary muscle for control (solid lines) and for the following: I_{CaL} block by 70–80-90% in simulations and by 1 (*A, top*) and 3 μM (*A, bottom*) nisoldipine in experiments, I_{Ks} block by 90–100% in simulations and by 0.25 μM HMR-1556 in experiments (*B*), I_{K1} block by 80–90% in simulations and by 30 μM BaCl$_2$ in experiments (*C*), and I_{Kr} block by 100% in simulations and by 0.1 μM dofetilide in experiments (*D*). All experimental curves represent average over experiments. Values for percent changes in the time constant of the fast phase of APD rate adaptation (τ_{fast}) induced by each intervention are also shown.

larization, respectively). Despite the enhancement of AP triangulation associated with large τ_{fast} values, no afterdepolarizations were observed in the simulations for 60% changes in τ_f, τ_{xs}, I_{CaL} maximal conductance, and I_{Ks} maximal conductance, although a 10-fold increase in τ_{fast} was obtained for a 60% reduction in τ_f.

Regarding the slow phase of APD adaptation, Fig. 6 shows that I_{NaK} inhibition results in an increase in τ_{slow} and also an increased ρ and δ, suggesting the increased likelihood of EAD generation (24, 27, 42). Indeed, I_{NaK} inhibition by 30% in simulations and by 0.6 μM strophanthin G in experiments results in an increase in δ from 1.11 to 1.15 and from 1.20 to
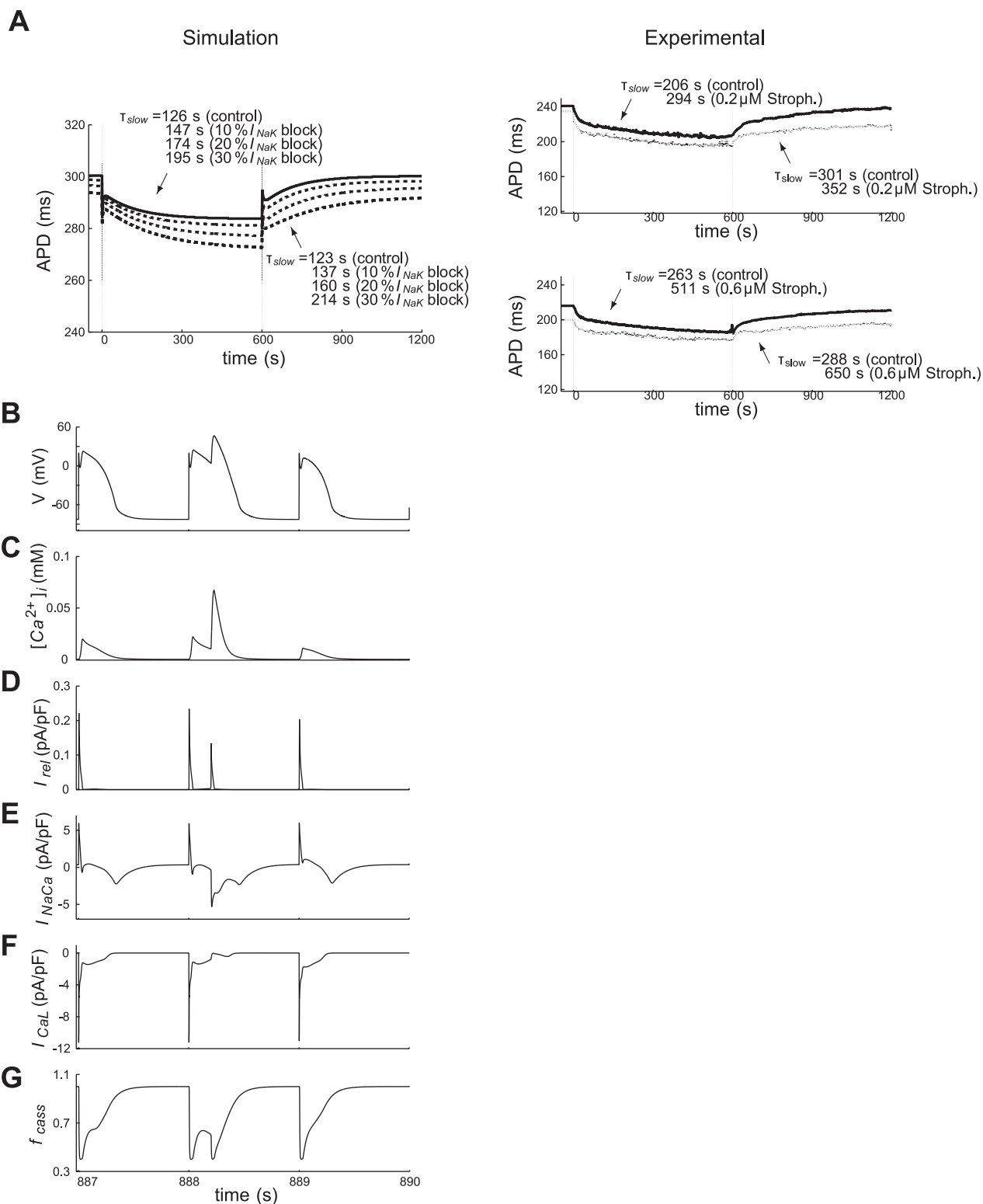
Fig. 8. *A*: effect of Na$^+$/K$^+$ pump inhibition on the slow phase of APD rate adaptation. *A*: simulated (*left*) and experimental (*right*) APD adaptation in control (solid line) and for Na$^+$/K$^+$ pump inhibition (dotted line) by 10–20-30% in simulated human ventricular cardiomyocytes and by 0.2 (*top*) and 0.6 μM (*bottom*) strophanthin G (Stroph) in canine experiments. Experimental curves represent average over experiments. *B*: early afterdepolarization generated following CL increase from 600 to 1,000 ms for simulated 60% I_{NaK} inhibition. *C–G*: corresponding time course of [Ca^{2+}]$_i$, I_{rel}, I_{NaCa}, I_{CaL}, and calcium-dependent inactivation gate f_{cass} of I_{CaL}. See main text for definitions of abbreviations. V, voltage.

1.33, respectively. EADs are observed in the simulations for I_{NaK} inhibition by 60% following HR deceleration, for all cell types in both humans and dogs. An example of EADs under those conditions in a simulated human ventricular myocyte is shown in Fig. 8B. Increasing the degree of I_{NaK} inhibition > 35% results in a significant increase in τ_{slow}: $\tau_{slow} = 380$ s and 1,610 s for 35 and 40% of I_{NaK} inhibition, respectively. In addition, I_{NaK} inhibition degrees > 40% lead to oscillations in APD adaptation dynamics and EADs, which prevent its characterization using exponential functions. Based on our results, APD rate adaptation is defined as protracted when associated $\tau_{slow} > 380$ s. The mechanisms of EAD formation are the same in both humans and dogs: severe I_{NaK} inhibition results in an increase in $[Na^+]_i$ levels, and thus in I_{NaCa}-mediated calcium influx (Fig. 8C), which increases $[Ca^{2+}]_i$ and calcium release from the sarcoplasmic reticulum (I_{rel}, Fig. 8D). This gives rise to the enhanced depolarizing current via I_{NaCa} and I_{CaL} (Fig. 8, E–G) and, consequently, EAD formation.

DISCUSSION

The clinical relevance of ventricular rate adaptation has been emphasized in a number of studies (15, 22, 45) and is highlighted by the frequent involvement of sudden changes in CL in the initiation of lethal arrhythmias. In the present study, a synergistic combination of theoretical and experimental methods is used to investigate the ionic basis of QTI and APD HR adaptation and their link to proarrhythmic mechanisms. Simulation predictions on QTI and APD adaptation dynamics in humans were validated using experimental and clinical data available in the literature, and key ionic mechanisms of ventricular HR adaptation in humans were identified. Because of limitations in the availability of human tissue and similarities in repolarization mechanisms in humans and dogs, further investigations of the ionic basis of ventricular HR adaptation were performed using a combination of simulations and experiments in humans and dogs. The results show that both QTI and APD HR adaptation follow similar dynamics, consisting of two phases, fast and slow, driven by I_{CaL} and I_{Ks} kinetics and conductances, and $[Na^+]_i$ dynamics and I_{NaK}, respectively. Our results suggest that protracted QTI rate adaptation (defined by $\tau_{slow} > 380$ s), as measured from the surface ECG of patients at high arrhythmic risk, could be a reflection of adverse ionic changes involving I_{CaL}, I_{Ks}, and $[Na^+]_i$ dynamics that, upon further deterioration, may facilitate arrhythmia initiation via an increased likelihood of EAD generation.

Dynamics and Mechanisms of Ventricular HR Adaptation in Humans

This study shows that simulated QTI and APD HR adaptation dynamics in humans are in good qualitative and quantitative agreement with the results reported in experimental and clinical studies (3, 18, 22, 29, 35, 36). The simulation results report two phases, fast and slow, in QTI and APD adaptation dynamics, as previously reported in human experiments (18, 29, 35, 36) and also confirmed in experiments performed in this study. The time constants for the two phases in human are $\tau_{fast} < 30$ s and $\tau_{slow} \geq 2$ min, respectively, in both simulations and experiments, in this study and in the literature (18, 36). Similar adaptation dynamics are found in dogs, with a slightly longer adaptation time compared with that in humans.

Our simulation results identify I_{CaL} and I_{Ks} properties as the main ionic determinants of the fast rate-dependent APD changes in humans, with I_{CaL} inactivation (Fig. 5A) playing a major role, as reported in previous studies for humans (31), for guinea pigs and rabbits (39), and for canine Purkinje fibers (6). In addition, our results show that I_{Ks} activation kinetics also contribute to the fast rate-dependent APD shortening (Fig. 5A), as previously suggested (8, 13, 14).

Importantly, we also demonstrate that $[Na^+]_i$ dynamics play a key role in the slow phase of APD adaptation (Fig. 5). I_{NaK} inhibition, as it occurs in ischemia and heart failure patients, results in slower $[Na^+]_i$ dynamics and delayed APD accommodation. The importance of I_{NaK} in the slow phase of APD adaptation was previously suggested in animal species such as dogs and guinea pigs (6, 10, 11, 14) but not in humans. Our study quantifies it and confirms it for humans. In addition, we show that it is primarily due to the role of I_{NaK} in regulating $[Na^+]_i$ dynamics, and, indirectly, $[Ca^{2+}]_i$ dynamics through the Na^+/Ca^{2+} exchanger, rather than to alterations in the electrogenic I_{NaK} current.

Ventricular rate adaptation as an indicator of arrhythmic risk. Following a thorough validation of the simulated rate adaptation dynamics described in *Ventricular Rate Adaptation*, computer simulations were used to explore the link between protracted HR adaptation and increased arrhythmic risk, as previously suggested (22, 35). The main preclinical arrhythmic risk biomarkers, namely, AP triangulation, probability of I_{CaL} reactivation, and APDR, were evaluated for conditions that lead to delayed APD adaptation, to quantify risk of occurrence of repolarization instabilities such as EADs and/or alternans (5, 44).

As discussed in *Ventricular Rate Adaption*, delayed APD adaptation could be caused by an increase in τ_{fast} (via a moderate reduction in τ_f or τ_{xs} or severe I_{CaL} maximal conductance block) or in τ_{slow} (via I_{NaK} inhibition). Reduced τ_f values have been reported in dogs with chronic atrioventricular block (1), which exhibit a high propensity for EADs and Torsades de Pointes, whereas reduced τ_{xs} is caused by a mutation in the KCNQ1 gene that causes short QT syndrome and is associated with high sudden cardiac death rate (4). Our simulations also show that a less-pronounced initial APD rate adaptation is associated with an increased AP triangulation and, in the case of reduced τ_{xs}, a higher probability of I_{CaL} reactivation, which facilitates EAD formation (25, 27, 30). Our results are also consistent with experimental results showing that the low incidence of EADs observed following the administration of amiodarone could be related to the ability of the drug to slow I_{CaL} (43) and decrease τ_{fast}. Furthermore, in patients who benefit from amiodarone therapy, the efficacy of the drug has been explained by its ability to accelerate QTI rate adaptation (37).

Reduced τ_f or τ_{xs}, and therefore increased τ_{fast}, are also associated with APDR slopes flattening, consistent with previous studies (23). The potential of APDR slopes as arrhythmic risk predictors is somewhat controversial. Both experimental and theoretical studies have shown that steep restitution slopes facilitate a spiral wave breakup and a transition from ventricular tachycardia to fibrillation (20, 32). However, conditions associated with flat restitution slopes also allow wave break (9, 16) and could favor reentrant wave stability (17, 19). Thus large τ_{fast} values could also be associated with an increased

arrhythmic risk due to the increased likelihood of the establishment of reentrant activity.

Both our simulation and experimental results show that I_{NaK} plays a key role in determining τ_{slow}. Large τ_{slow} due to I_{NaK} inhibition is associated with an increase in AP triangulation and in the likelihood of I_{CaL} reactivation (Fig. 6), indicating an increased risk of EAD formation. Large τ_{slow} values are also associated with flat APDR slopes, which could favor the stability of reentrant circuits and thus could increase arrhythmic risk.

Our simulations show that, both in humans and dogs, EADs develop for 60% I_{NaK} inhibition, a degree of inhibition observed in ischemic disease and heart failure patients treated with digitalis (7). In the experiments of I_{NaK} inhibition with 0.2 or 0.6 μM strophanthin G performed in the present study, no EADs were observed; however, the degree of drug-induced I_{NaK} inhibition is unknown and may be below 60%. Additionally, the lack of EADs in the experiments might be explained by the electrophysiological differences between the experimental (canine papillary muscle) and simulated preparations (canine Epi and human Endo/Mid/Epi tissue).

Limitations of the Study

In our study, a human ventricular model was used to explore ventricular rate adaptation dynamics and simulation predictions were validated using experimental and clinical data from the literature and in a limited set of experiments in humans performed in this study. Additional experiments and simulations were performed in dogs because of its similarities with humans in repolarization mechanisms. Our experimental and theoretical results obtained in dogs and humans are qualitatively similar, although quantitative differences exist that could be due to true animal species differences, differences in experimental conditions, or model limitations. First, differences exist in I_{K1} and I_{Ks} in canine versus human cardiac ventricular tissue (28), which would lead to differences in ventricular rate adaptation. Second, the human model (38) does not include a description of the late sodium current and its I_{Ks} conductance was defined based on APD measurements, which could explain a larger contribution of I_{Ks} to APD adaptation in simulations compared with experiments. Despite these limitations, the present study provides new insights into the mechanisms of ventricular rate adaptation and its link to proarrhythmic risk in humans through a challenging combination of theoretical and experimental work.

DISCLOSURES

No conflicts to disclose.

REFERENCES

1. **Antoons G, Volders PG, Stankovicova T, Bito V, Stengl M, Vos MA, Sipido KR.** Window Ca^{2+} current and its modulation by Ca^{2+} release in hypertrophied cardiac myocytes from dogs with chronic atrioventricular block. *J Physiol* 579: 147–160, 2007.
2. **Arnold L, Page J, Attwell D, Cannell M, Eisner DA.** The dependence on heart rate of the human ventricular action potential duration. *Cardiovasc Res* 16: 547–551, 1982.
3. **Attwell D, Cohen I, Eisner DA.** The effects of heart rate on the action potential of guinea-pig and human ventricular muscle. *J Physiol* 313: 439–461, 1981.
4. **Bélocq C, van Ginneken AC, Bezzina CR, Alders M, Escande D, Mannens MM, Baró I, Wilde AA.** Mutation in the KCNQ1 gene leading to the short QT-interval syndrome. *Circulation* 109: 2394–2397, 2004.
5. **Binah O, Rosen MR.** Mechanisms of ventricular arrhythmias. *Circulation* 85: I25–I31, 1992.
6. **Boyett MR, Fedida D.** Changes in the electrical activity of dog cardiac Purkinje fibres at high heart rates. *J Physiol* 350: 361–391, 1984.
7. **Bundgaard H, Kjeldsen K.** Human myocardial Na,K-ATPase concentration in heart failure. *Mol Cell Biochem* 163–164: 277–283, 1996.
8. **Carmeliet E.** Action potential duration, rate of stimulation, and intracellular sodium. *J Cardiovasc Electrophysiol* 17: S2–S7, 2006.
9. **Clayton RH, Taggart P.** Regional differences in APD restitution can initiate wavebreak and re-entry in cardiac tissue: a computational study. *Biomed Eng Online* 20: 4–54, 2005.
10. **Decker KF, Heijman J, Silva JR, Hund TJ, Rudy Y.** Properties and ionic mechanisms of action potential adaptation, restitution, and accommodation in canine epicardium. *Am J Physiol Heart Circ Physiol* 296: H1017–H1026, 2009.
11. **Drake AJ, Noble MI, Schouten V, Seed A, Ter Keurs HE, Wohlfart B.** Is action potential duration of the intact dog heart related to contractility or stimulus rate? *J Physiol* 331: 499–510, 1982.
12. **Drouin E, Charpentier F, Gauthier C, Laurent K, Le Marec H.** Electrophysiologic characteristics of cells spanning the left ventricular wall of human heart: evidence for presence of M cells. *J Am Coll Cardiol* 26: 185–192, 1995.
13. **Eisner DA, Dibb KM, Trafford AW.** The mechanism and significance of the slow changes of ventricular action potential duration following a change of heart rate. *Exp Physiol* 94: 520–528, 2009.
14. **Faber GM, Rudy Y.** Action potential and contractility changes in $[Na^+]_i$ overloaded cardiac myocytes: a simulation study. *Biophys J* 78: 2392–2404, 2000.
15. **Fenichel RR, Malik M, Antzelevitch C, Sanguinetti M, Roden DM, Priori SG, Ruskin JN, Lipicky RJ, Cantilena LR; Independent Academic Task Force.** Drug-induced torsades de pointes and implications for drug development. *J Cardiovasc Electrophysiol* 15: 475–495, 2004.
16. **Fenton FH, Evans SJ, Hastings HM.** Memory in an excitable medium: a mechanism for spiral wave breakup in the low-excitability limit. *Phys Rev Lett* 83: 3964–3967, 1999.
17. **Frame LH, Simson MB.** Oscillations of conduction, action potential duration, and refractoriness. A mechanism for spontaneous termination of reentrant tachycardias. *Circulation* 78: 1277–1287, 1988.
18. **Franz MR, Swerdlow CD, Liem LB, Schaefer J.** Cycle length dependence of human action potential duration in vivo. Effects of single extrastimuli, sudden sustained rate acceleration and deceleration, and different steady-state frequencies. *J Clin Invest* 82: 972–979, 1988.
19. **Franz MR.** The electrical restitution curve revisited: steep or flat slope—which is better? *J Cardiovasc Electrophysiol* 14: S140–S147, 2003.
20. **Garfinkel A, Kim YH, Voroshilovsky O, Qu Z, Kil JR, Lee MH, Karagueuzian HS, Weiss JN, Chen PS.** Preventing ventricular fibrillation by flattening cardiac restitution. *Proc Natl Acad Sci USA* 97: 6061–6066, 2000.
21. **Gima K, Rudy Y.** Ionic current basis of electrocardiographic waveforms: a model study. *Circ Res* 90: 889–896, 2002.
22. **Grom A, Faber TS, Brunner M, Bode C, Zehender M.** Delayed adaptation of ventricular repolarization after sudden changes in heart rate due to conversion of atrial fibrillation. A potential risk factor for proarrhythmia? *Europace* 7: 113–121, 2005.
23. **Gudzenko V, Shiferaw Y, Savalli N, Vyas R, Weiss JN, Olcese R.** Influence of channel subunit composition on L-type Ca^{2+} current kinetics and cardiac wave stability. *Am J Physiol Heart Circ Physiol* 293: H1805–H1815, 2007.
24. **Guo D, Zhao X, Wu Y, Liu T, Kowey PR, Yan GX.** L-type calcium current reactivation contributes to arrhythmogenesis associated with action potential triangulation. *J Cardiovasc Electrophysiol* 18: 196–203, 2007.
25. **Guo D, Zhou J, Zhao X, Gupta P, Kowey PR, Martin J, Wu Y, Liu T, Yan GX.** L-type calcium current recovery versus ventricular repolariza-

tion: preserved membrane-stabilizing mechanism for different QT intervals across species. *Heart Rhythm* 5: 271–279, 2008.

26. **Hao SC, Christini DJ, Stein KM, Jordan PN, Iwai S, Bramwell O, Markowitz SM, Mittal S, Lerman BB.** Effect of β-adrenergic blockade on dynamic electrical restitution in vivo. *Am J Physiol Heart Circ Physiol* 287: H390–H394, 2004.

27. **Hondeghem LM, Carlsson L, Duker G.** Instability and triangulation of the action potential predict serious proarrhythmia, but action potential duration prolongation is antiarrhythmic. *Circulation* 103: 2004–2013, 2001.

28. **Jost N, Varró A, Szuts V, Kovacs PP, Seprényi GY, Biliczki P, Lengyel Cs Prorok J, Bitay M, Ördög B, Szabad J, Varga-Orvos Z, Puskas L, Cotella D, Papp JG, Virag L, Nattel S.** Molecular basis of repolarization reserve differences between dogs and man (Abstract). *Circulation* 118: S342, 2008.

29. **Lau CP, Freedman AR, Fleming S, Malik M, Camm AJ, Ward DE.** Hysteresis of the ventricular paced QT interval in response to abrupt changes in pacing rate. *Cardiovasc Res* 22: 67–72, 1988.

30. **Lawrence CL, Pollard CE, Hammond TG, Valentin JP.** Nonclinical proarrhythmia models: predicting Torsades de Pointes. *J Pharmacol Toxicol Methods* 52: 46–59, 2005.

31. **Li GR, Yang B, Feng J, Bosch RF, Carrier M, Nattel S.** Transmembrane I_{Ca} contributes to rate-dependent changes of action potentials in human ventricular myocytes. *Am J Physiol Heart Circ Physiol* 276: H98–H106, 1999.

32. **Mahajan A, Sato D, Shiferaw Y, Baher A, Xie LH, Peralta R, Olcese R, Garfinkel A, Qu Z, Weiss JN.** Modifying L-type calcium current kinetics: consequences for cardiac excitation and arrhythmia dynamics. *Biophys J* 94: 411–423, 2008.

33. **Martínez JP, Almeida R, Olmos S, Rocha AP, Laguna P.** A wavelet-based ECG delineator: evaluation on standard databases. *IEEE Trans Biomed Eng* 51: 570–581, 2004.

34. **Milberg P, Reinsch N, Wasmer K, Mönnig G, Stypmann J, Osada N, Breithardt G, Haverkamp W, Eckardt L.** Transmural dispersion of repolarization as a key factor of arrhythmogenicity in a novel intact heart model of LQT3. *Cardiovasc Res* 65: 397–404, 2005.

35. **Pueyo E, Smetana P, Caminal P, de Luna AB, Malik M, Laguna P.** Characterization of QT interval adaptation to RR interval changes and its use as a risk-stratifier of arrhythmic mortality in amiodarone-treated survivors of acute myocardial infarction. *IEEE Trans Biomed Eng* 51: 1511–1520, 2004.

36. **Seed WA, Noble MI, Oldershaw P, Wanless RB, Drake-Holland AJ, Redwood D, Pugh S, Mills C.** Relation of human cardiac action potential duration to the interval between beats: implications for the validity of rate corrected QT interval (QTc). *Br Heart J* 57: 32–37, 1987.

37. **Smetana P, Pueyo E, Hnatkova K, Batchvarov V, Laguna P, Malik M.** Individual patterns of dynamic QT/RR relationship in survivors of acute myocardial infarction and their relationship to antiarrhythmic efficacy of amiodarone. *J Cardiovasc Electrophysiol* 15: 1147–1154, 2004.

38. **ten Tusscher KH, Panfilov AV.** Alternans and spiral breakup in a human ventricular tissue model. *Am J Physiol Heart Circ Physiol* 291: H1088–H1100, 2006.

39. **Tolkacheva EG, Anumonwo JM, Jalife J.** Action potential duration restitution portraits of mammalian ventricular myocytes: role of calcium current. *Biophys J* 91: 2735–2745, 2006.

40. **Varró A, Baláti B, Iost N, Takács J, Virág L, Lathrop DA, Csaba L, Tálosi L, Papp JG.** The role of the delayed rectifier component I_{Ks} in dog ventricular muscle and Purkinje fibre repolarization. *J Physiol* 523: 67–81, 2000.

41. **Virág L, Acsai K, Hála O, Zaza A, Bitay M, Bogáts G, Papp JG, Varró A.** Self-augmentation of the lengthening of repolarization is related to the shape of the cardiac action potential: implications for reverse rate dependency. *Br J Pharmacol* 156: 1076–1084, 2009.

42. **Viswanathan PC, Rudy Y.** Pause induced early afterdepolarizations in the long QT syndrome: a simulation study. *Cardiovasc Res* 42: 530–542, 1999.

43. **Wegener FT, Ehrlich JR, Hohnloser SH.** Dronedarone: an emerging agent with rhythm- and rate-controlling effects. *J Cardiovasc Electrophysiol* 17: S17–S20, 2006.

44. **Weiss JN, Qu Z, Chen PS, Lin SF, Karagueuzian HS, Hayashi H, Garfinkel A, Karma A.** The dynamics of cardiac fibrillation. *Circulation* 112: 1232–1240, 2005.

45. **Zaza A, Malfatto G, Schwartz PJ.** Sympathetic modulation of the relation between ventricular repolarization and cycle length. *Circ Res* 68: 1191–1203, 1991.